Available online at www.sciencedirect.com
ScienceDirect
Trans. Nonferrous Met. Soc. China 34(2024) 465−479
Transactions of Nonferrous Metals Society of China
www.tnmsc.cn

Effect of Al−10Nb−3Ce−2.5B inoculant on microstructures, damping and tensile mechanical properties of Zn−Al eutectoid alloy

Jian-jun ZHANG[1], Fu-xing YIN[2], Hui YU[1], Pu-guang JI[1], Li LIU[1], Yu-fang LI[1], Zhi-xian JIAO[1], Qing-zhou WANG[1]

1. Tianjin Key Laboratory of Materials Laminating Fabrication and Interface Control Technology, School of Materials Science and Engineering, Hebei University of Technology, Tianjin 300130, China;
2. Institute of New Materials, Guangdong Academy of Sciences, Guangzhou 510651, China

Received 5 September 2022; accepted 17 March 2023

Abstract: A novel Al−10Nb−3Ce−2.5B inoculant was prepared, and its effect on microstructures, damping and tensile mechanical properties of Zn−Al eutectoid (ZA22) alloy was systematically studied. It was found that the inoculant had an effective refining effect on the α-phase in the ZA22 alloy (α-phase could be refined to 16 μm), and the morphology of the α-phase could also change from coarse dendrite to small petal. Orientation relationships (ORs) between the α-phase and the CeB_6 and NbB_2 particles in the inoculant were established by the edge−edge matching model (E2EM), and based on the E2EM, the refining mechanism of the inoculant on the ZA22 alloy was revealed. Compared with the uninoculated ZA22 alloy, the high temperature damping of the inoculated ZA22 alloy, especially the damping peak arising from the reverse eutectoid transformation, was significantly improved. Moreover, the room temperature tensile mechanical properties of the inoculated ZA22 alloy were also significantly improved. The tensile strength and elongation of the ZA22 alloy with the best refining effect were 18.56% and 119.04% higher than those of the unrefined ZA22 alloy, respectively. Correlated mechanisms were discussed.

Key words: Zn−Al eutectoid alloy; inoculant; microstructure refinement; damping; tensile mechanical property

1 Introduction

Zn−Al eutectoid (ZA22) alloy has become an indispensable high-quality material in the engineering field due to its good wear resistance, extensive raw material sources, low melting energy consumption and easy processability [1−4]. In particular, this alloy also has a high damping property that is not affected by magnetic field, which makes it often used for vibration and noise reduction of electromechanical components [5−7]. However, due to the coarse dendrites, the mechanical properties of this alloy are still relatively low, which makes it unable to meet the mechanical requirements of damping components used in specific places [8−11]. Therefore, how to significantly improve the mechanical properties of this alloy without reducing the high damping capacity has become an urgent problem to be resolved.

Refinement by inoculants is one of the potential ways to improve the mechanical properties of ZA22 alloy [12−15]. As a commonly used inoculant, Al−5Ti−B has made an extremely important contribution to the microstructure refinement and comprehensive property improvement of ZA22 alloy. Al_3Ti and TiB_2 intermetallic compound particles in the Al−5Ti−B inoculant can serve as efficient heterogeneous nucleation centers of α-phase in the ZA22 alloy, leading to the significant refinement of the alloy [13]. LUO et al [14] also studied the effects of trace Sc and Zr on microstructures of ZA22 alloy, and found that Al_3Sc, Al_3Zr and Al_3(Sc, Zr) intermetallic compound

Corresponding author: Qing-zhou WANG, Tel: +86-13821156527, E-mail: qzwang@hebut.edu.cn
DOI: 10.1016/S1003-6326(23)66411-8

particles also had positive effects on the microstructure refinement of ZA22 alloy. In addition, SAFWAN and ADNAN [15] reported that the addition of Ti−B−Mo to ZA22 alloy resulted in a decrease in grain size and changes in the microstructures, leading to an increase in the strain hardening index of the alloy. However, the above refiners cannot significantly improve the mechanical properties of ZA22 alloy. Therefore, it is necessary to further explore other effective refiners of ZA22 alloy.

In recent years, many researchers have used niobium borides and rare earth borides to refine the microstructures and improve the mechanical properties of Al alloys [16−19]. DING et al [16] reported the positive refining effect of niobium diboride (NbB_2) particles on Al−Cu−Mn alloy, and they found that after refining the grains the ultimate tensile strength, yield strength and elongation of the alloy could be increased to 514 MPa, 361 MPa and 11.5% from the original 435 MPa, 291 MPa and 8.4%, respectively. ZHUO et al [17] calculated the surface energy, adhesion work, charge density difference, and partial density of states of a specific NbB_2/Al interface by using density functional theory based on the first-principles method. Based on the crystallography and thermodynamics, they demonstrated the effectiveness of NbB_2 particles as efficient heterogeneous nucleation substrates for Al grains. LIU et al [18−20] used transmission electron microscopy (TEM) to study the microstructure of the CeB_6/Al interface in Al−Ce−B alloys. They found that a well-bonded interface was formed between CeB_6 and the Al matrix, suggesting that CeB_6 particles could also be used as efficient heterogeneous nucleation substrates for Al grains. Furthermore, they found that by adding 0.3 wt.% CeB_6/Al inoculant ribbon, the grain size of pure Al could be significantly reduced, and the mechanical properties were remarkably improved.

To sum up, niobium borides and rare earth borides have efficient refining effect on the grains of Al alloys and can significantly improve their mechanical properties. It is reasonable to believe that these two borides can also effectively refine the α-phase in ZA22 alloy, and can significantly improve the mechanical properties. However, up to now, there are still no relevant research reports. Therefore, in this study, a novel Al−10Nb−3Ce−2.5B inoculant containing CeB_6 and NbB_2 particles was prepared, and its effects on microstructures, damping and tensile mechanical properties of ZA22 alloy were systematically investigated. This study can provide an important theoretical basis for the research and development of high strength and high damping Zn−Al alloys.

2 Experimental

2.1 Preparation of Al−10Nb−3Ce−2.5B inoculant and inoculated ZA22 alloys

Al−10Nb−3Ce−2.5B (wt.%) inoculant was fabricated in a vacuum arc furnace by using commercial Al−60Nb, Al−20Ce and Al−3B master alloys as raw materials (XU et al [21] studied various mass ratios of Nb to B in Al−Nb−B master alloys and proposed that 10:1 was the optimal ratio. This ratio was adopted in the present study. In addition, the mass ratio of Ce to B was set to be 2:1 to achieve an molar ratio of 1:6. Therefore, when the contents of Nb and Ce in the inoculant were set to be 10 wt.% and 3 wt.%, respectively, the content of B was 2.5 wt.%). The button ingots were smelted for at least 5 times to ensure sufficient reaction and homogenization of components in the inoculant.

The ZA22 alloy was smelted in an electric resistance furnace at 650 °C under the protection of argon by using high-purity Zn and Al metals (purity is higher than 99.9 wt.%) as raw materials. When the raw materials were melted, different mass fractions of Al−10Nb−3Ce−2.5B inoculant (0.05 wt.%, 0.15 wt.%, 0.25 wt.%, 0.35 wt.% and 0.45 wt.%) were added. After stirring and standing, the melt was poured into a cylindrical steel mould with a diameter of 20 mm and a depth of 150 mm.

2.2 Structure characterization

The microstructures were observed by optical microscope (OM, BX41M Olympus) and field emission scanning electron microscopy (FESEM, Quanta 450 FEG) equipped with an energy dispersive spectrometer (EDS). Before observation, the specimens were ground with grit papers and polished with flannelette, and then etched by the solution of 1% HF. The size of α-phase in the ZA22 alloy was measured by using the linear intercept method through the SISC IAS V8.0 image software. Element mapping was obtained by using electron probe microanalysis (EPMA, JEOL 8530F). Phase identification was carried out by using X-ray

diffractometer (XRD, Bruker D8 Discover) with Cu K_α radiation within the 2θ range from 10° to 90°.

2.3 Performance test

Internal friction (IF), $\tan\delta$, was used to characterize the damping property, and it was measured on dynamic mechanical analyzer (DMA, Q800) by using the method of forced vibration over a wide temperature range from room temperature to 400 °C. The heating rate was 5 °C/min and the measuring frequency was 0.5 Hz. Tensile test was performed on universal testing machine (UTM, INSTRON) with a deformation rate of 2 mm/min at room temperature. The tensile specimens with a gauge length of 25 mm and a cross-section of *d*5 mm were machined according to the GB/T 228.1—2010 (ISO 6892:1998) standard [22]. At least three specimens were measured for each alloy to ensure the repeatability of the results.

3 Results and discussion

3.1 Characterization of Al−10Nb−3Ce−2.5B inoculant

From the XRD pattern shown in Fig. 1, it can be seen that four intermetallic phases (CeB_6, NbB_2, $Al_{11}Ce_3$ and Al_3Nb) are formed in the Al−10Nb−3Ce−2.5B inoculant. It is apparent that the peak intensities of CeB_6 and NbB_2 are much higher than those of $Al_{11}Ce_3$ and Al_3Nb. The contents of these four phases in the inoculant were calculated by using the reference intensity ratio (RIR) value method, and the results are listed in Table 1.

Figures 2(a)−(c) show the SEM images of the Al−10Nb−3Ce−2.5B inoculant. Combined with the EPMA analysis results shown in Figs. 2(a′)−(c′), it can be determined that the particles in Figs. 2(a)−(c) are NbB_2, CeB_6 and CeB_6+NbB_2+$Al_{11}Ce_3$+Al_3Nb, respectively. In addition, it is worth noting that trace amount of rare earth Ce element can be detected near the NbB_2 particles in Fig. 2(a). Combined with the XRD analysis results shown in Fig. 1, the phase containing Ce can be identified as $Al_{11}Ce_3$. Of course, it is also possible that the rare earth element Ce is enriched on the surface of the NbB_2 particles. From the distribution characteristics of various intermetallic compound particles in Fig. 2, it can be seen that there are a large number of NbB_2 and CeB_6 particles in the inoculant, and the distribution of these two kinds of particles has obvious solitary characteristics (Figs. 2(a) and (b)). The coexistence of four intermetallic compound particles can only be seen in a few places (Fig. 2(c)). Compared with NbB_2 and CeB_6 particles, the amount of Al_3Nb particles is very small. These results confirm the conclusions drawn from the XRD patterns. There is no significant difference in morphology and size between NbB_2 and CeB_6 particles. It is difficult to identify them without the EPMA analysis. In addition, from Fig. 2, it can be seen that the size of most particles is 1−10 μm. According to our previous work [12,13], the suitable particle size for the refinement of ZA22 alloy should be around 1 μm.

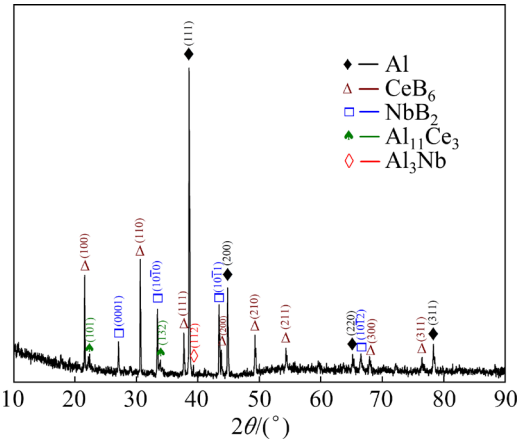

Fig. 1 XRD pattern of Al−10Nb−3Ce−2.5B inoculant

Table 1 Contents of various phases in Al−10Nb−3Ce−2.5B inoculant calculated by RIR value method

Phase	Content/wt.%	Content/vol.%
Al	73.62	84.46
CeB_6	12.33	7.97
NbB_2	9.2	4.11
$Al_{11}Ce_3$	3.2	2.33
Al_3Nb	1.65	1.13

3.2 Microstructure evolution of inoculated ZA22 alloy

Figure 3 shows the optical images of inoculated ZA22 alloy. It can be seen from Fig. 3(a) that the α-phase in the original ZA22 alloy is dendritic, and its size can reach 100 μm. The microstructure characteristics of the original ZA22 alloy have been introduced in detail in our previous work [12]. It can be seen from Figs. 3(b)−(f) that the Al−10Nb−3Ce−2.5B inoculant has significant

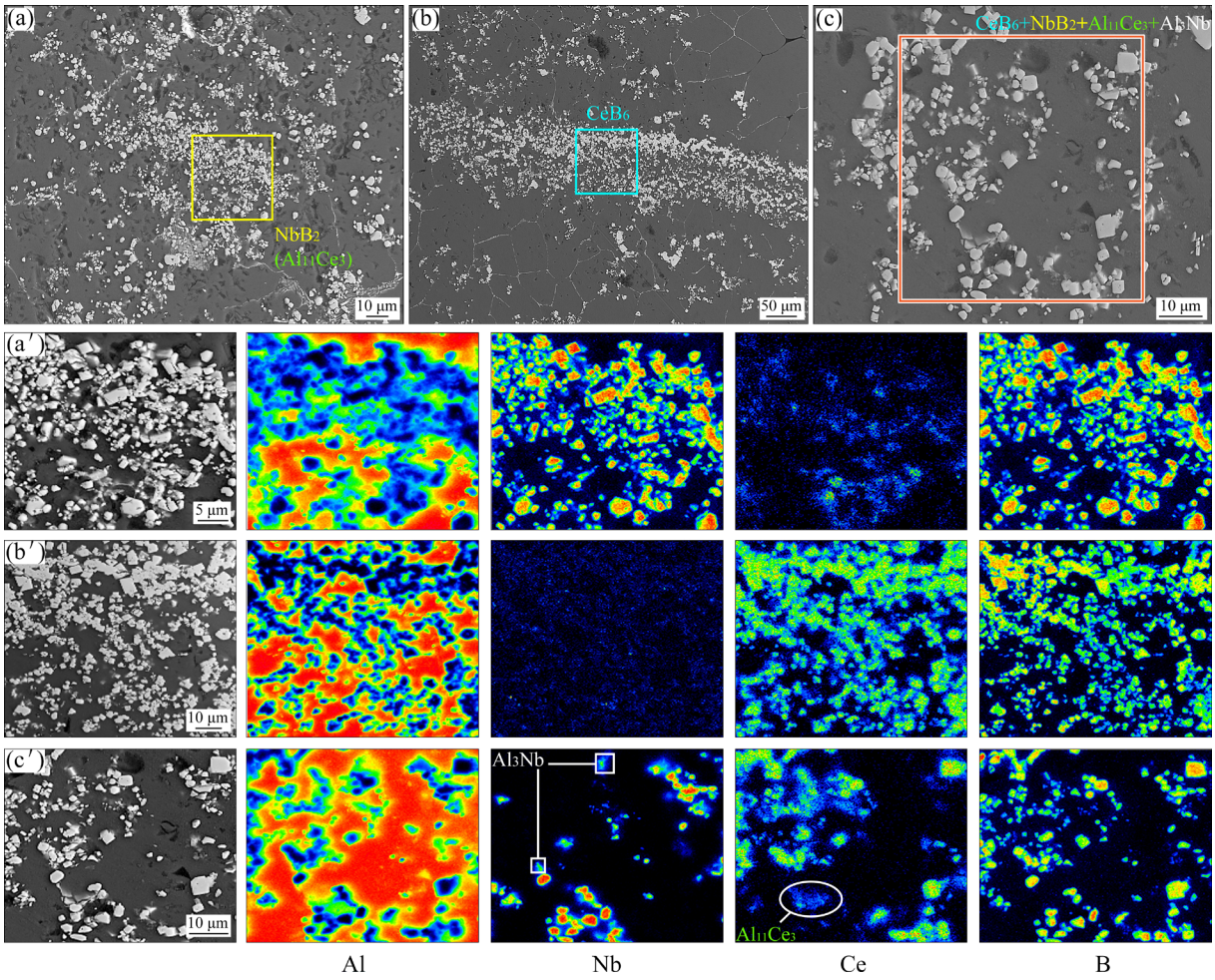

Fig. 2 (a−c) SEM images of Al−10Nb−3Ce−2.5B inoculant; (a′−c′) EPMA analysis results of marked regions in (a), (b) and (c), respectively

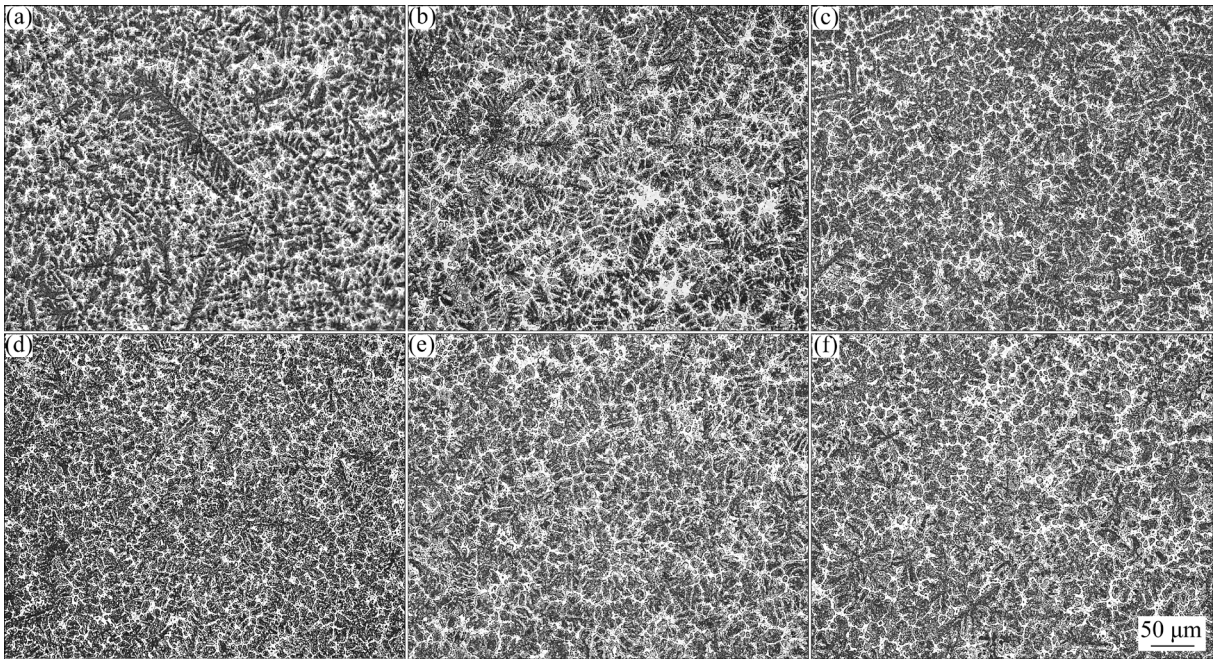

Fig. 3 Optical images of ZA22 alloys refined by different contents of inoculant: (a) 0; (b) 0.05 wt.%; (c) 0.15 wt.%; (d) 0.25 wt.%; (e) 0.35 wt.%; (f) 0.45 wt.%

refining effect on the α-phase in the ZA22 alloy, and with increasing the content of inoculant, the size of the α-phase decreases first and then increases (see Fig. 4). When the inoculant content reaches 0.25 wt.%, the best refining effect can be obtained, and the average size of the α-phase is about 16 μm. With the decrease of size, the morphology of α-phase also undergoes a change from coarse dendrite to fine petal crystal.

Figure 5 shows the lamellar eutectoid structures of the original and inoculated ZA22 alloys. By comparing, it can be found that the lamellar spacing in eutectoid structure of the inoculated alloy is obviously smaller than that of the original alloy. That is, the lamellar eutectoid structure of the inoculated ZA22 alloy is also refined.

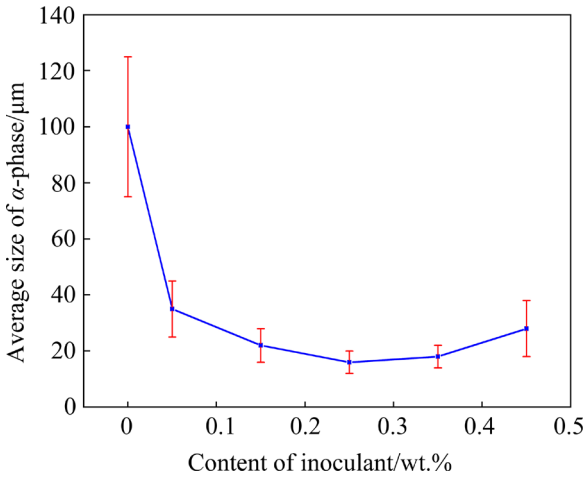

Fig. 4 Average size of α-phase in ZA22 alloys refined by different contents of inoculant

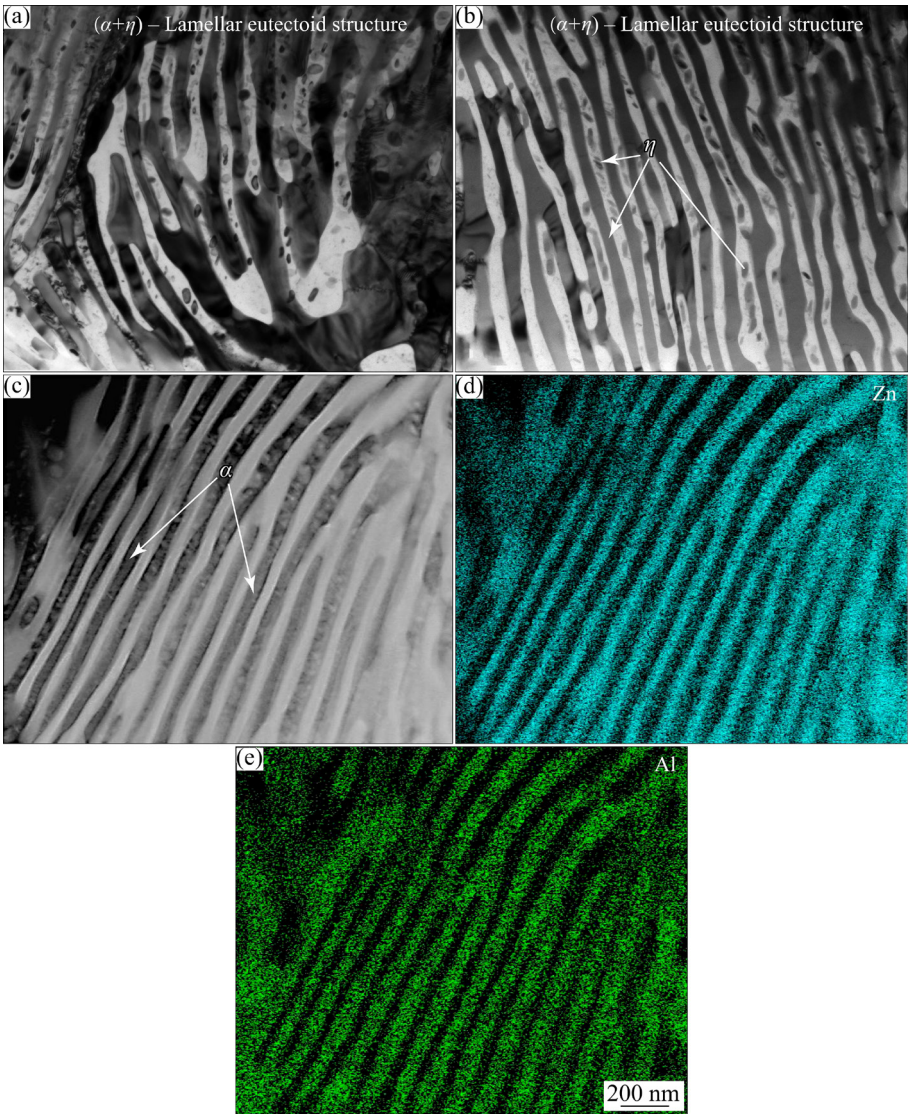

Fig. 5 (a) TEM image of lamellar eutectoid structure in original ZA22 alloy; (b, c) TEM and HAADF-STEM images of lamellar eutectoid structure in ZA22 alloy refined by 0.25 wt.% inoculant, respectively; (d, e) Distribution maps of Zn and Al elements in (c), respectively

This is understandable: when the α-phase is refined, the β-phase formed through the peritectic reaction (L+α→β) is also refined. Since the lamellar eutectoid structure is formed through the eutectoid transformation (β→α+η), it is also refined. In addition, from Fig. 5 it can be found that there are some gray granular precipitates between the lamellae of eutectoid structure. According to the element distribution shown in Figs. 5(d) and 5(e), they can be identified as η-phase. The appearance of this granular η-phase should be due to the incomplete homogenization of the composition of the ZA22 alloy after the eutectoid transformation.

Figure 6 illustrates the EPMA analysis results of NbB_2 and CeB_6 intermetallic compound particles in the inoculated ZA22 alloy. From Figs. 6(a) and (b), it can be found that NbB_2 particles with an average size of 1 μm and different shapes are distributed in the α-phase. Similarly, Figs. 6(c) and (d) show CeB_6 particles with different shapes distributed in the α-phase, and the size is also maintained at about 1 μm. It can be concluded that although intermetallic compound particles in the inoculant shown in Fig. 2 have a wide size range, only the particles with a size of about 1 μm play an active role in the refinement of the ZA22 alloy. Based on the distribution characteristics of the two intermetallic compound particles in the α-phase, it can be confirmed that they have the potential of being efficient heterogeneous nucleation centers of the α-phase. Of course, this still needs crystallographic evidence. It is worth noting that from the EPMA results of NbB_2 shown in Fig. 6(b), it can be found that a trace amount of Ce element is detected on the surface of the particle, which is in accordance with the result shown in Fig. 2(a). It is reasonable to speculate that the surface of some NbB_2 particles is enriched with Ce element. Due to the relatively low contents of $Al_{11}Ce_3$ and Al_3Nb in the inoculant, and the small amount (0.25 wt.%) of the inoculant, it is really difficult to find them in the inoculated ZA22 alloy (It does not mean that they do not exist). The positive effects of $Al_{11}Ce_3$ and Al_3Nb phases on the microstructure of the ZA22 alloy can be inferred from the results reported by other researchers [12,16,23].

An interesting phenomenon is shown in Fig. 7. From the regions indicated by red boxes in Fig. 7(a), it is found that there is a black phase in the center of NbB_2 particles, which is similar to the core−shell structure. According to the corresponding energy spectrum shown in Fig. 7(b), Al and Nb elements can be detected at the core position of this special NbB_2 particle. In addition, we also find this

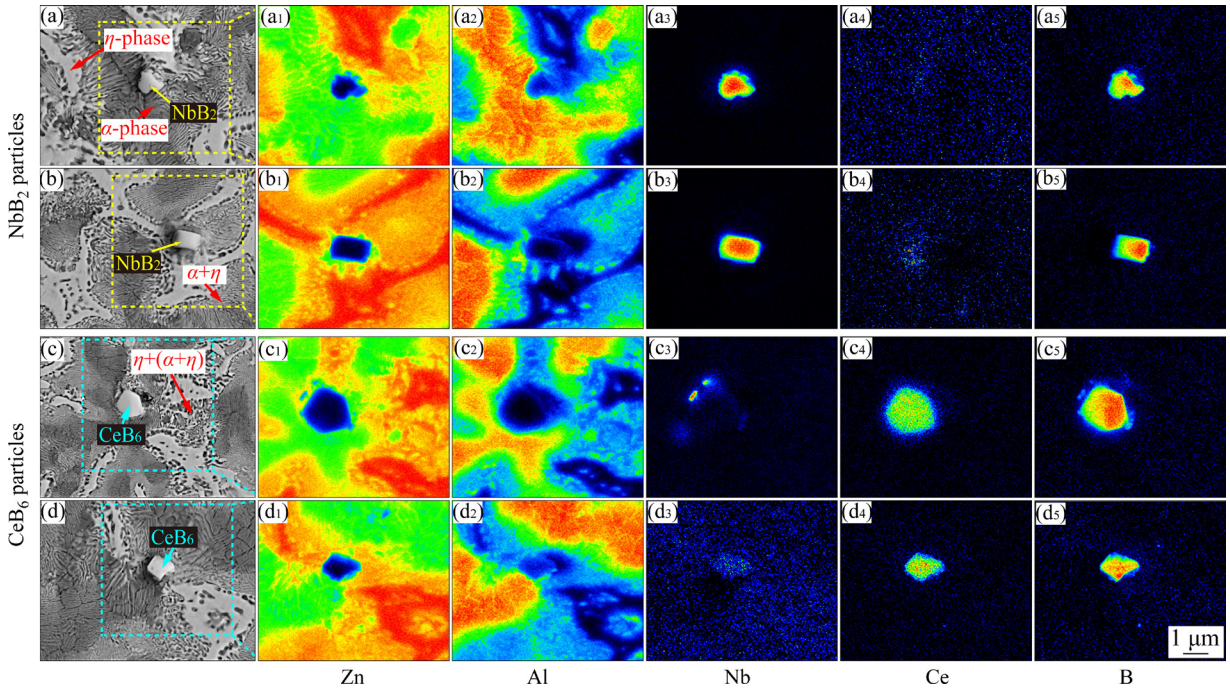

Fig. 6 EPMA analysis results of ZA22 alloy refined by 0.25 wt.% inoculant: (a, b) NbB_2 particles in inoculated ZA22 alloy; (a_1−a_5) Element distribution maps of (a); (b_1−b_5) Element distribution maps of (b); (c, d) CeB_6 particles in inoculated ZA22 alloy; (c_1−c_5) Element distribution maps of (c); (d_1−d_5) Element distribution maps of (d)

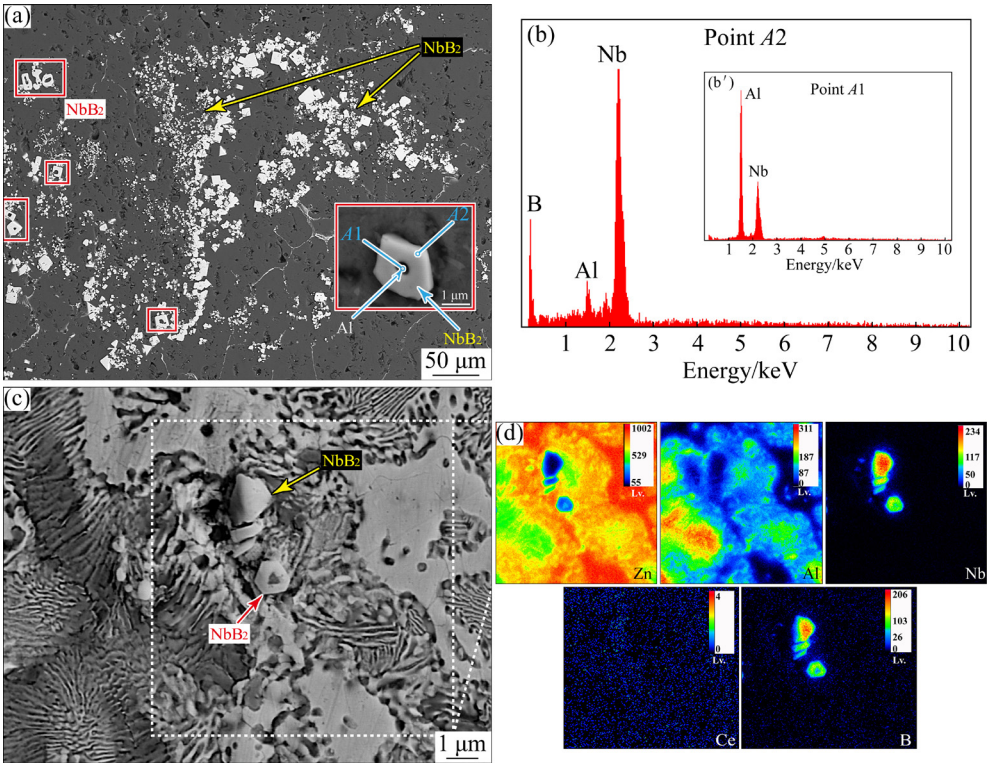

Fig. 7 (a) SEM image of NbB_2 particles in Al−10Nb−3Ce−2.5B inoculant; (b) EDS analysis results of Points *A*1 and *A*2 marked in (a); (c) SEM image of NbB_2 particles in ZA22 alloy refined by 0.45 wt.% inoculant; (d) EPMA analysis results of region indicated by white box in (c)

core−shell structure in the ZA22 alloy refined by 0.45 wt.% inoculant, as shown in Fig. 7(c), which shows the universality of the existence of this core−shell structure in the inoculant. According to the EPMA analysis results shown in Fig. 7(d), it can be seen that the periphery of the core−shell structure is rich in Nb and B elements, and the center is rich in Al and Nb elements. We believe that the core of this core−shell structure in this study should be mainly composed of α-phase, and the detected Nb element should come from the surrounding NbB_2 phase. In order to reveal the formation mechanism of the core−shell structure, the thermodynamic reaction processes during the fabrication of the Al−10Nb−3Ce−2.5B inoculant were analyzed. The following chemical reactions may occur:

$$Nb+B\rightarrow NbB_2 \quad (1)$$

$$Ce+B\rightarrow CeB_6 \quad (2)$$

$$Al+B\rightarrow AlB_2 \quad (3)$$

$$Al+Nb\rightarrow Al_3Nb \quad (4)$$

$$Al_3Nb+AlB_2\rightarrow NbB_2+4Al \quad (5)$$

$$Al+Ce\rightarrow Al_{11}Ce_3 \quad (6)$$

The Gibbs free energy change (ΔG) curves of the above reactions calculated by the HSC Chemistry software are shown in Fig. 8. It can be inferred from the figure that during the fabrication of inoculant, Reactions (1)−(4) can all take place, among which Reaction (2) is most likely to take place, followed by Reaction (1). Therefore, considering the influence of element contents, the content of CeB_6 in the inoculant should be the highest, followed by NbB_2, which is in good accordance with the result shown in Table 1. Reaction (6) can only take place below 1000 °C, so the content of $Al_{11}Ce_3$ in the inoculant is lower than that of CeB_6 and NbB_2. Only when the temperature is higher than 1000 °C, Reaction (5) will take place. So Reaction (5) should not be the primary mechanism for the formation of the core−shell structure. This structure is most likely formed by Reaction (1) that takes places surrounding the liquid Al during solidification. Reaction (5) was also reported by other researchers [23,24], which results in the reduction of the content of Al_3Nb phase and the absence of AlB_2 phase in the inoculant. Remarkably, from Fig. 7(c) we can see that

0.45 wt% inoculant causes the segregation of NbB_2 particles, which explains why the refining effect will decrease after adding excess inoculant, as shown in Figs. 3 and 4.

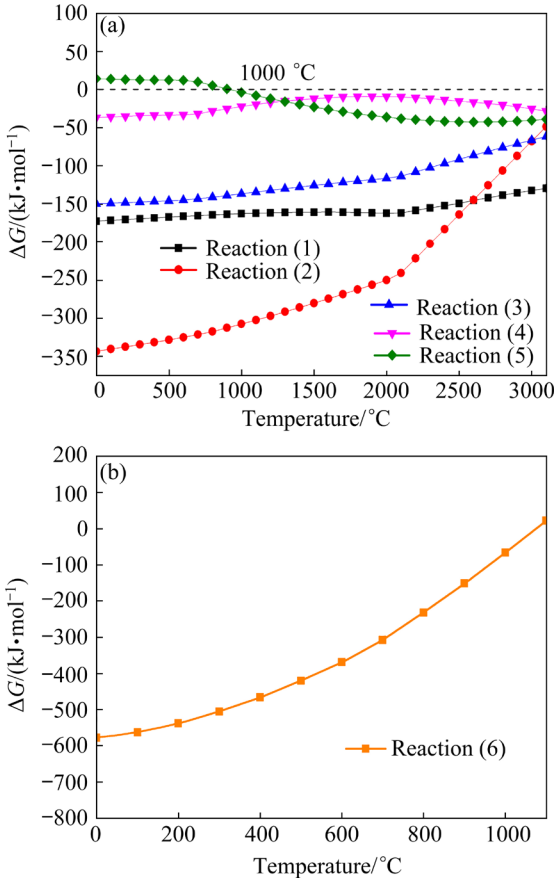

Fig. 8 Gibbs free energy change (ΔG) curves of reactions in Al−10Nb−3Ce−2.5B inoculant calculated by HSC Chemistry software: (a) Reactions (1)−(5); (b) Reaction (6)

3.3 Orientation relationships (ORs) between refiners and α-phase

Based on the edge−edge matching crystallographic model (E2EM) [25], the condition that Phase A can act as the effective heterogeneous nucleation center of Phase B is that they must have a certain OR, the interplanar spacing misfit (f_p) of parallel crystal planes should be less than 6%, and the interatomic spacing misfit (f_a) of parallel crystal directions should be less than 10%. The f_p and f_a are defined by Eqs. (7) and (8), respectively [26]:

$$f_p = \frac{|R_B - R_A|}{R_A} \tag{7}$$

$$f_a = \frac{|D_B - D_A|}{D_A} \tag{8}$$

where R_A and R_B are the interplanar spacings of Phase A and Phase B, respectively, and D_A and D_B are the interatomic spacings of Phase A and Phase B, respectively.

The α-phase in the ZA22 alloy has a face-centered cubic (FCC) structure. According to the results reported by other researchers [27], the lattice constant of the α-phase can be taken as 0.4050 nm in the present study. Its closely packed crystal planes are {111}, and near closely packed crystal planes are {200} and {220}. The interplanar spacings of these three planes are 0.23383, 0.20250 and 0.14319 nm, respectively. Its closely packed crystal directions are ⟨110⟩, and near closely packed crystal directions are ⟨100⟩ and ⟨112⟩, respectively. The atomic spacings of these three directions are 0.2863, 0.4050 and 0.4960 nm, respectively. The CeB_6 phase has a simple cubic crystal structure and its lattice parameters meet the relationship of a=b=c=0.4141 nm. Its closely packed crystal planes are {111}, and near closely packed crystal planes are {100} and {110}. The interplanar spacings of these three planes are 0.23908, 0.41410 and 0.29281 nm, respectively. Its closely packed crystal directions are ⟨110⟩, and near closely packed crystal directions are ⟨100⟩ and ⟨111⟩. The interatomic spacings of these three directions are 0.5856, 0.4141 and 0.7172 nm, respectively. The interplanar spacing misfits and the interatomic spacing misfits between the α-phase and CeB_6 are listed in Tables 2 and 3, respectively.

The possible matching crystal planes between the α-phase and CeB_6 include $\{111\}_\alpha/\{111\}_{CeB_6}$, $\{200\}_\alpha/\{100\}_{CeB_6}$ and $\{220\}_\alpha/\{110\}_{CeB_6}$, and the possible matching crystal directions include $\langle 110\rangle_\alpha/\langle 110\rangle_{CeB_6}$ and $\langle 100\rangle_\alpha/\langle 100\rangle_{CeB_6}$. If a possible matching

Table 2 Interplanar spacing mismatch between α-phase and CeB_6 phase

α	CeB_6	f_p
{111}	{111}, {100}, {110}	2.24, 77.09, 25.22
{200}	{111}, {100}, {110}	18.06, 2.24, 44.59
{220}	{111}, {100}, {110}	16.51, 44.59, 2.24

Table 3 Interatomic spacing mismatch between α-phase and CeB_6 phase

α	CeB_6	f_a
⟨110⟩	⟨110⟩, ⟨100⟩, ⟨111⟩	2.24, 44.59, 25.22
⟨100⟩	⟨110⟩, ⟨100⟩, ⟨111⟩	44.599, 2.24, 77.09
⟨112⟩	⟨110⟩, ⟨100⟩, ⟨111⟩	18.06, 16.51, 44.59

crystal plane together with a possible matching crystal direction can form a group of OR, this crystal direction must be located on the crystal plane. Therefore, the possible ORs between the α-phase and CeB_6 can be predicted as follows: $\{111\}_\alpha//\{111\}_{CeB_6}$, $\langle 110\rangle_\alpha//\langle 110\rangle_{CeB_6}$; $\{200\}_\alpha//\{100\}_{CeB_6}$, $\langle 110\rangle_\alpha//\langle 110\rangle_{CeB_6}$; $\{200\}_\alpha//\{100\}_{CeB_6}$, $\langle 100\rangle_\alpha//\langle 100\rangle_{CeB_6}$; $\{220\}_\alpha//\{110\}_{CeB_6}$, $\langle 110\rangle_\alpha//\langle 110\rangle_{CeB_6}$; $\{220\}_\alpha//\{110\}_{CeB_6}$, $\langle 100\rangle_\alpha//\langle 100\rangle_{CeB_6}$. The schematic diagrams of lattice matching are shown in Fig. 9.

The NbB_2 phase has a hexagonal structure and its lattice parameters meet the relationship of $a=b=0.3111$ nm and $c=0.3274$ nm. Its closely and near closely packed planes include $\{10\bar{1}1\}$, $\{10\bar{1}0\}$, $\{0001\}$ and $\{11\bar{2}0\}$. The interplanar spacing of these planes are 0.2080, 0.2693, 0.3274 and

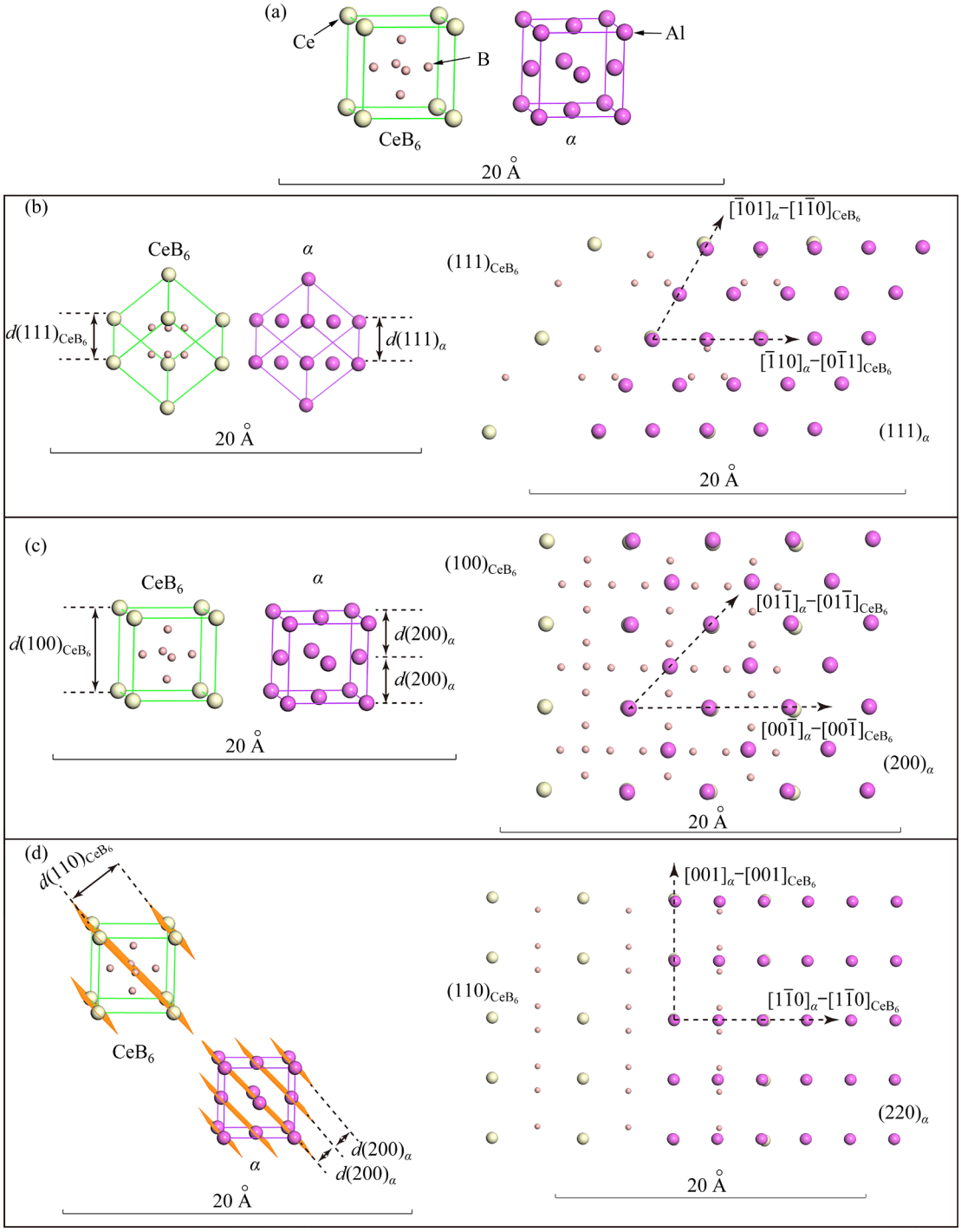

Fig. 9 Schematic diagrams of lattice matching between α-phase and CeB_6 phase: (a) Crystal structures of α-phase and CeB_6 phase; (b) Lattice matching between α (111) and CeB_6 (111) crystal planes; (c) Lattice matching between α (200) and CeB_6 (100) crystal planes; (d) Lattice matching between α (220) and CeB_6 (110) crystal planes

0.1555 nm, respectively. Its closely packed and near closely packed crystal directions include $\langle 11\bar{2}0\rangle$, $\langle 0001\rangle$, $\langle \bar{1}\,\bar{1}23\rangle$ and $\langle 10\,\bar{1}0\rangle$, and their interatomic spacings are 0.3111, 0.3274, 0.4516 and 0.5388 nm, respectively. The interplanar spacing misfits and the interatomic spacing misfits between the α-phase and NbB_2 are listed in Tables 4 and 5, respectively.

The possible matching crystal planes between the α-phase and NbB_2 include $\{200\}_\alpha$/$\{10\,\bar{1}1\}_{NbB_2}$ and $\{220\}_\alpha$/$\{10\,\bar{1}0\}_{NbB_2}$, and the possible matching crystal directions include $\langle 110\rangle_\alpha$/ $\{11\bar{2}0\}_{NbB_2}$, $\langle 110\rangle_\alpha$/$\{10\,\bar{1}0\}_{NbB_2}$, $\langle 112\rangle_\alpha$/$\langle \bar{1}\,\bar{1}23\rangle_{NbB_2}$, and $\langle 112\rangle_\alpha$/ $\langle 10\,\bar{1}0\rangle_{NbB_2}$. The possible ORs between the α-phase and NbB_2 can be predicted as follows: $\{200\}_\alpha$// $\{10\,\bar{1}1\}_{NbB_2}$, $\langle 110\rangle_\alpha$//$\{11\bar{2}0\}_{NbB_2}$; $\{220\}_\alpha$// $\{10\,\bar{1}0\}_{NbB_2}$, $\langle \bar{1}10\rangle_\alpha$//$\{11\bar{2}0\}_{NbB_2}$; $\{220\}_\alpha$// $\{10\,\bar{1}0\}_{NbB_2}$, $\langle 112\rangle_\alpha$/$\langle \bar{1}\,\bar{1}23\rangle_{NbB_2}$. The schematic diagrams of lattice matching are shown in Fig. 10.

Table 4 Interplanar spacing mismatch between α-phase and NbB_2 phase

α	NbB_2	f_p
{111}	$\{10\,\bar{1}1\}$, $\{10\,\bar{1}0\}$, {0001}, $\{11\bar{2}0\}$	11.045, 15.171, 40.018, 33.497
{200}	$\{10\,\bar{1}1\}$, $\{10\,\bar{1}0\}$, {0001}, $\{11\bar{2}0\}$	2.716, 32.990, 61.679, 23.209
{220}	$\{10\,\bar{1}1\}$, $\{10\,\bar{1}0\}$, {0001}, $\{11\bar{2}0\}$	45.262, 5.96, 128.649, 8.597

Table 5 Interatomic spacing mismatch between α-phase and NbB_2 phase

α	NbB_2	f_a
$\langle 110\rangle$	$\langle 11\bar{2}0\rangle$, $\langle 0001\rangle$, $\langle \bar{1}\,\bar{1}23\rangle$, $\langle 10\,\bar{1}0\rangle$	8.632, 14.324, 57.705, 5.920
$\langle 100\rangle$	$\langle 11\bar{2}0\rangle$, $\langle 0001\rangle$, $\langle \bar{1}\,\bar{1}23\rangle$, $\langle 10\,\bar{1}0\rangle$	23.185, 19.160, 11.514, 33.047
$\langle 112\rangle$	$\langle 11\bar{2}0\rangle$, $\langle 0001\rangle$, $\langle \bar{1}\,\bar{1}23\rangle$, $\langle 10\,\bar{1}0\rangle$	37.280, 33.994, 8.948, 8.632

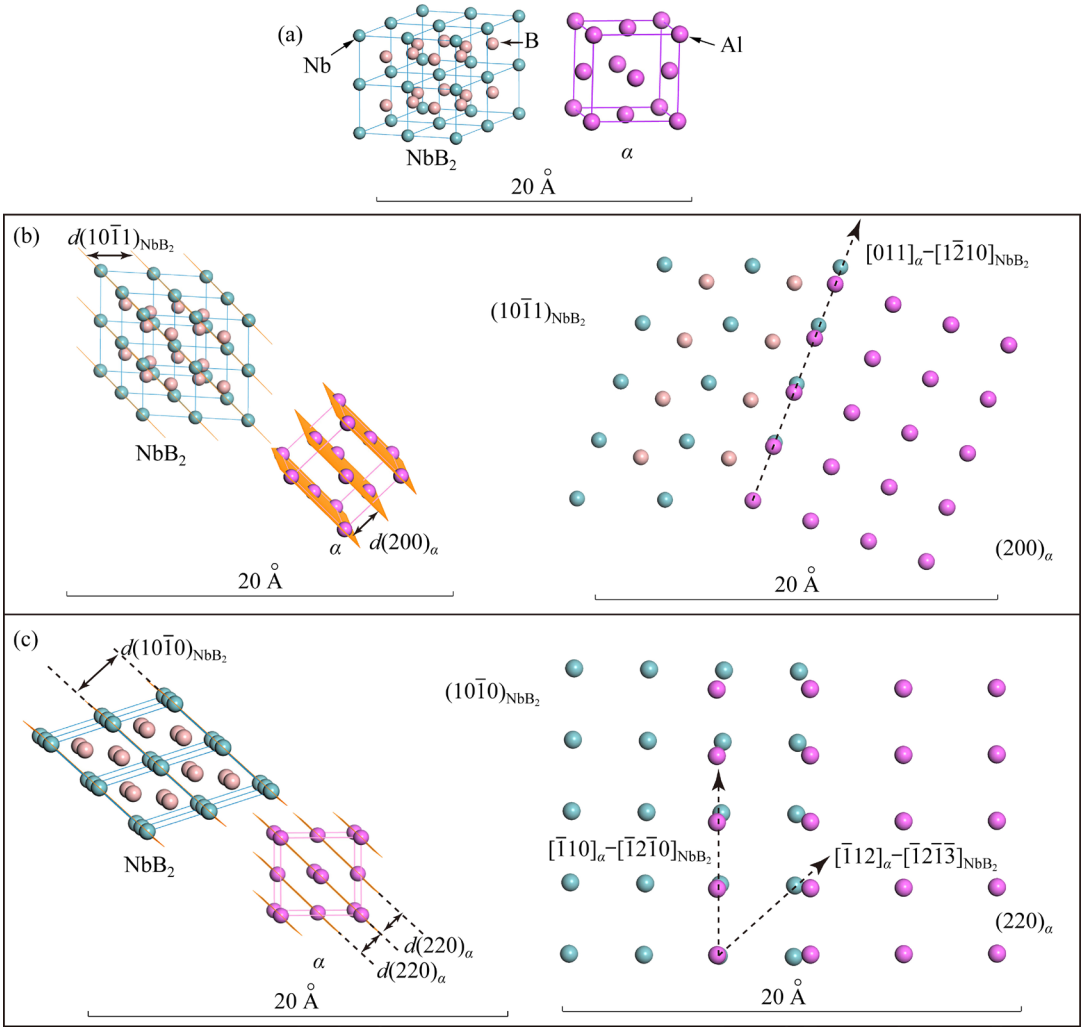

Fig. 10 Schematic diagrams of lattice matching between α-phase and NbB_2 phase: (a) Crystal structures of α-phase and NbB_2 phase; (b) Lattice matching between α (200) and NbB_2 $(10\,\bar{1}1)$ crystal planes; (c) Lattice matching between α (200) and NbB_2 $(10\,\bar{1}0)$ crystal planes

Figures 11 and 12 show the HAADF-STEM images and the selected area electron diffraction (SAED) patterns of CeB_6 and NbB_2 particles, respectively. According to the element distribution maps and SAED patterns, it is confirmed that the two particles are CeB_6 and NbB_2, respectively. In addition, it is found that the size of these two particles is around 1 μm, which is consistent with the result shown in Fig. 6. By analyzing the SAED patterns shown in Figs. 11(g) and 12(g), it is found that CeB_6, NbB_2 particles and α-phase have the following ORs: $(111)_{CeB_6}//(111)_\alpha$, and $(10\bar{1}1)_{NbB_2}//(200)_\alpha$. Obviously, this result belongs to one of the cases we predicted above.

3.4 Damping property of original and inoculated ZA22 alloys

Figure 13 shows the damping properties of the original and inoculated ZA22 alloys. Two damping peaks can be found at around 184 and 335 °C (hereafter as P1 and P2 peaks), respectively. The two peaks originate from the grain boundary relaxation and the reverse eutectoid transformation ($\alpha+\eta\rightarrow\beta$), respectively [12,13]. From the figure, it is apparent that at relatively low temperatures the damping of the original ZA22 alloy is slightly higher than that of the inoculated alloys. However, when the temperature is higher than 120 °C, the damping of inoculated alloys begins to be higher than that of the original alloy, and with further increasing the temperature, the difference between the damping values of the two kinds of alloys becomes larger and larger. In addition, for inoculated alloys, it is found that with increasing the content of inoculant, the damping increases first and then decreases. When 0.25 wt.% inoculant is added, the highest damping can be obtained.

The changes of damping in different ZA22 alloys are related to the changes of density and mobility of phase interfaces. For inoculated ZA22 alloys, although their interface density is increased, the mobility of interfaces is still low at low temperatures due to the low energy of interface atoms and the pinning effect of intermetallic compound particles. Moreover, the increase of interface density will increase the compressive stress between interfaces and further reduce their mobility [13]. With the increase of temperature, the

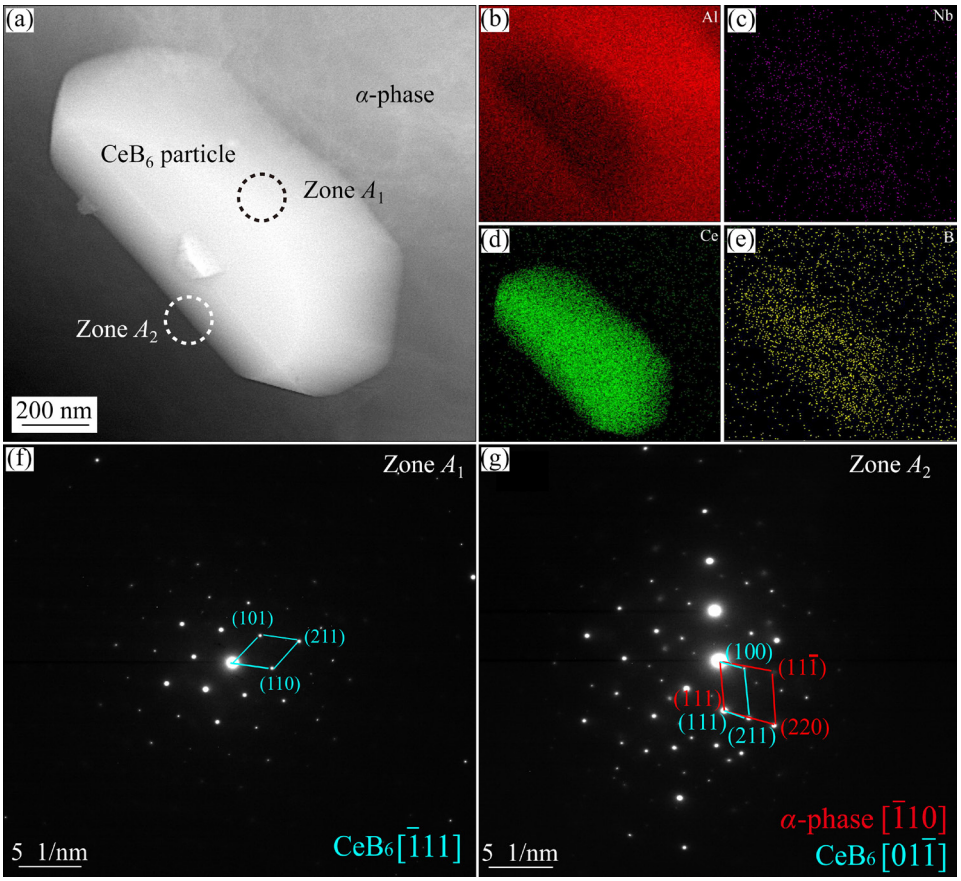

Fig. 11 (a) HAADF-STEM image of CeB_6 particle in ZA22 alloy refined by 0.25 wt.% inoculant; (b−e) Element distribution maps of (a); (f) SAED pattern of Zone A_1 marked in (a); (g) SAED pattern of Zone A_2 marked in (a)

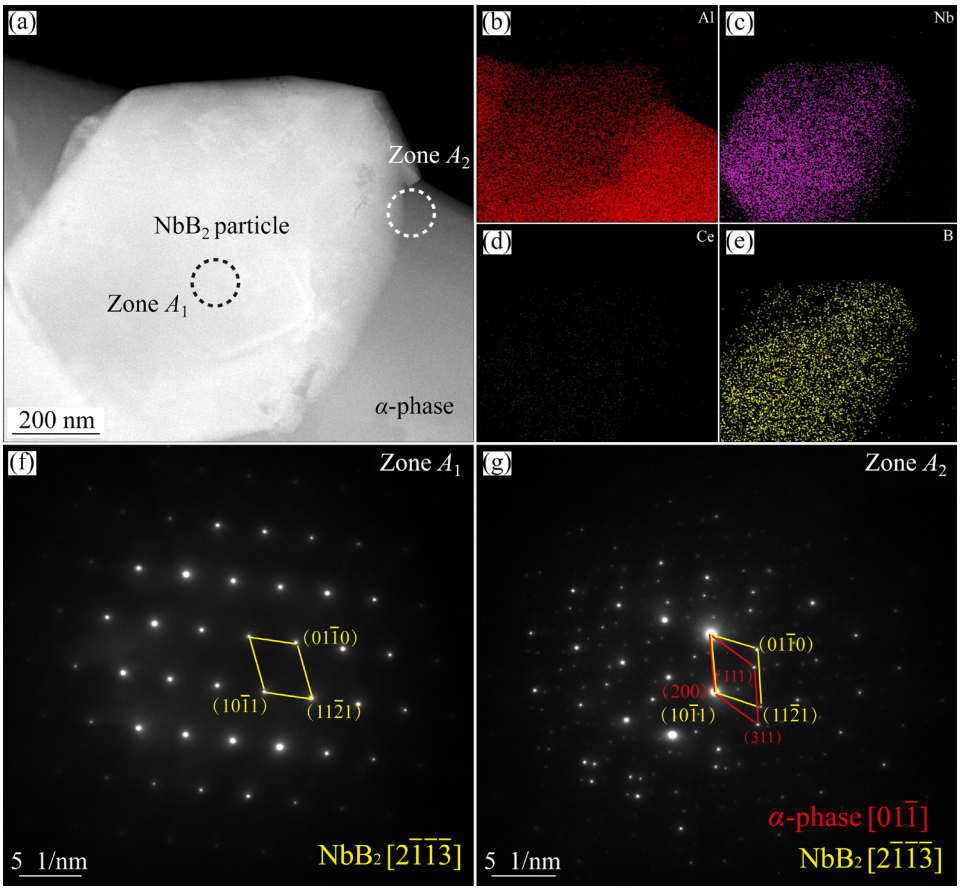

Fig. 12 (a) HAADF-STEM image of NbB_2 particle in ZA22 alloy refined by 0.25 wt.% inoculant; (b−e) Element distribution maps of (a); (f) SAED pattern of Zone A_1 marked in (a); (g) SAED pattern of Zone A_2 marked in (a)

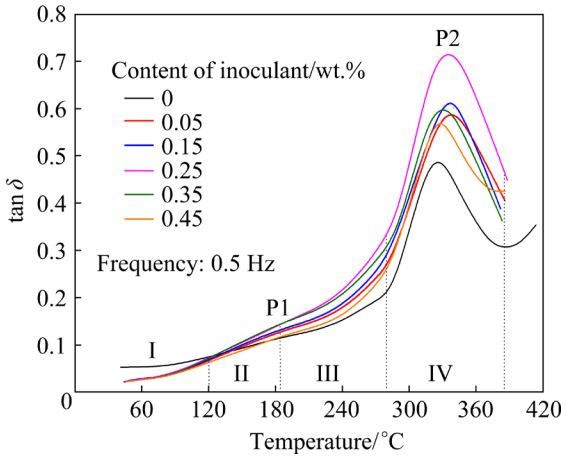

Fig. 13 Damping properties of original and inoculated ZA22 alloys

activity of interface atoms increases, which leads to the weakening of the pinning effect of intermetallic compound particles, thus increasing the mobility of interfaces. Therefore, when the temperature is higher than 120 °C, the damping of the inoculated alloy begins to be higher than that of the original alloy. When the temperature reaches 275 °C, the reverse eutectoid transformation begins to take place. It is understandable that the finer the α-phase, the higher the density of α/η, α/β and η/β interfaces during the reverse eutectoid transformation process, and the higher the P2 peak.

3.5 Tensile mechanical properties of original and inoculated ZA22 alloy

Figure 14 shows the tensile mechanical properties of the original and inoculated ZA22 alloys. It can be seen that the tensile mechanical properties (including tensile strength and elongation) of the inoculated alloys are superior to those of the original alloy, and with increasing the content of inoculant, the tensile mechanical properties of the inoculated alloys increase first and then decrease. When the content of inoculant reaches 0.25 wt.%, the highest tensile mechanical properties are obtained. The significant improvement in mechanical properties can be ascribed to the refinement of α-phase in the ZA22 alloy and the pinning effect of intermetallic compound particles

at the interfaces. In addition, the high-density α/η lamellar interfaces in the inoculated alloys will inhibit their mutual sliding due to the strong compressive stress between them, so the tensile strength increases with the increase of refining effect. The increase in ductility of the inoculated ZA22 alloy is mainly attributed to the significant reduction of the secondary dendrite arm size of the α-phase. The refinement of microstructure makes the distribution of applied stresses in the matrix more uniform during tensile tests. As a consequence, lager plastic deformation will take place before fracture, i.e., the ductility is improved.

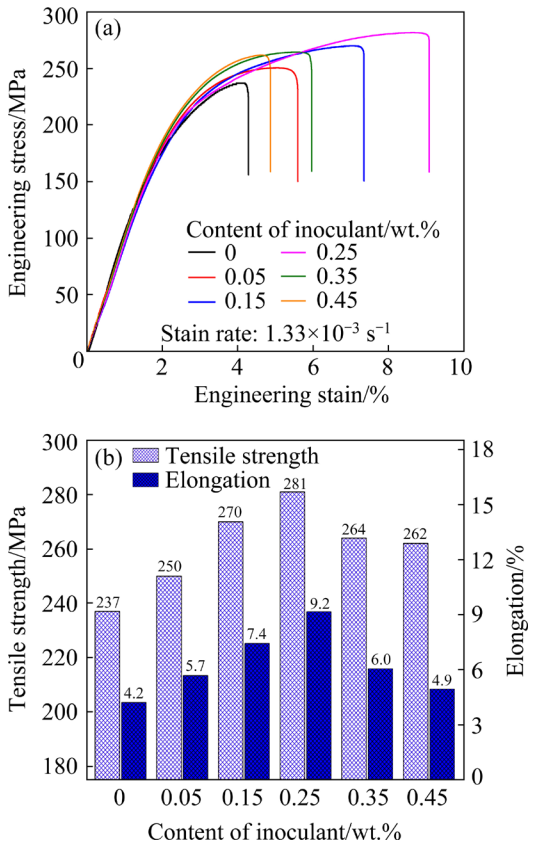

Fig. 14 Engineering stress−stain curves (a) and tensile mechanical properties (b) of original and inoculated ZA22 alloys

4 Conclusions

(1) Al−10Nb−3Ce−2.5B inoculant is mainly composed of CeB_6 and NbB_2 particles with particle size of 1−10 μm. It also contains a small amount of $Al_{11}Ce_3$ phase, Al_3Nb phase as well as special NbB_2(Al) core−shell structure. The Al−10Nb−3Ce−2.5B inoculant has significant refining effect on the α-phase in the ZA22 alloy, which can be attributed to the good ORs between the intermetallic compound particles (CeB_6 and NbB_2) in the inoculant and the α-phase. With increasing the content of inoculant, the size of α-phase decreases first and then increases. When the content of inoculant reaches 0.25 wt.%, the best refining effect is obtained. Excess inoculant will degrade the refining effect due to the segregation of NbB_2 particles.

(2) The high temperature damping of the inoculated ZA22 alloys is significantly improved compared with that of the original alloy, which originates from the competition between the improvement of damping caused by the increase of interface density and the decrease of damping caused by the decrease of interface mobility. When the temperature is lower than 120 °C, the decrease of interface mobility will become the main factor affecting damping, and the damping of the inoculated alloy will begin to be lower than that of the original alloy.

(3) The improvement of tensile strength of the inoculated ZA22 alloys can be attributed to the refinement of microstructures and the decrease of interface mobility, whereas, the superior ductility of the inoculated ZA22 alloys is due to the remarkable decrease of the secondary dendrite arm size of α-phase.

CRediT authorship contribution statement

Jian-jun ZHANG: Investigation, Data curation, Writing − Original draft; **Fu-xing YIN:** Writing − Reviewing & editing, Funding acquisition; **Hui YU:** Conceptualization; **Pu-guang JI:** Validation; **Li LIU:** Data curation; **Yu-fang LI:** Investigation; **Zhi-xian JIAO:** Investigation; **Qing-zhou WANG:** Conceptualization, Methodology, Project administration, Funding acquisition.

Declaration of competing interest

The authors declare that they have no known competing financial interests or personal relationships that could have appeared to influence the work reported in this paper.

Acknowledgments

This work was supported by the Guangdong Academy of Sciences, China (No. 2021GDASYL-20210102002), the Foundation Strengthening Program, China (No. 2019-JCJQ-ZD-142-00), and the Hebei

Province Graduate Innovation Funding Project, China (No. CXZZBS2022032).

References

[1] TORRES J H, ZHU Y H, HERRERA-VÁZQUEZ A, CASTAÑO V M. Strengthening of Zn−22Al−2Cu alloy wire by artificial ageing [J]. Materials Letters, 2000, 43: 153−157.

[2] LIU Ya-fei, YIN Fu-xing, YU Hui, FENG Jian-hang, JI Pu-guang, ZHANG Jian-jun, JIAO Zhi-xian, LIU Li, WANG Qing-zhou. Microstructural evolution, damping and tensile mechanical properties of multilayer Zn−22Al alloy fabricated by accumulative roll bonding (ARB) [J]. Materials Science and Engineering A, 2022, 840: 142911.

[3] YOUSEFI D, TAGHIABADI R, SHAERI M H. Effect of multi-pass multi-directional forging on tribological properties of Si-rich eutectoid ZA alloys [J]. Transactions of Nonferrous Metals Society of China, 2021, 31: 2024−2038.

[4] TANAKA T, TAKIGAWA Y, HIGASHI K. Effect of temperature on the cavity nucleation rate for fine-grained Zn−22wt.%Al alloy [J]. Scripta Materialia, 2008, 58: 643−646.

[5] WEI J N, WANG D Y, XIE W J, LUO J L, HAN F S. Effects of macroscopic graphite particulates on the damping behavior of Zn−Al eutectoid alloy [J]. Physics Letters A, 2007, 366: 134−136.

[6] YU Si-rong, LIU Jia-an, LUO Yan-ru, LIU Yao-hui. Compressive behavior and damping property of ZA22/SiC_p composite foams [J]. Materials Science and Engineering A, 2007, 457: 325−328.

[7] DEMIRTAS M, ATLI K C, YANAR H, PURCEK G. Effect of grain refinement and phase composition on room temperature superplasticity and damping capacity of dual-phase Zn−Al alloys [J]. Journal of Materials Research, 2018, 33: 1032−1045.

[8] CHO T S, LEE H J, AHN B, KAWASAKI M, LANGDON T G. Microstructural evolution and mechanical properties in a Zn−Al eutectoid alloy processed by high-pressure torsion [J]. Acta Materialia, 2014, 72: 67−79.

[9] DEMIRTAS M, PURCEK G, YANAR H, ZHANG Z J, ZHANG Z F. Effect of different processes on lamellar-free ultrafine grain formation, room temperature superplasticity and fracture mode of Zn−22Al alloy [J]. Journal of Alloys and Compounds, 2016, 663: 775−783.

[10] CETIN M E, DEMIRTAS M, SOFUOGLU H, CORA Ö N, PURCEK G. Effects of grain size on room temperature deformation behavior of Zn−22Al alloy under uniaxial and biaxial loading conditions [J]. Materials Science and Engineering A, 2016, 672: 78−87.

[11] YU S, LI W, HE Z. Study on tensile strengths of Al_2O_3 short fiber reinforced Zn−Al alloy composites at elevated temperatures [J]. Journal of Alloys and Compounds, 2007, 431: L8−L11.

[12] ZHANG Jian-jun, WANG Qing-zhou, JIAO Zhi-xian, YIN Fu-xing, CUI Chun-xiang, YAO Chang. Effects of combined use of inoculation and modification heat treatment on microstructure, damping and mechanical properties of Zn−Al eutectoid alloy [J]. Materials Science and Engineering A, 2020, 790: 139740.

[13] LI Nan, LIU Xiao-jin, WANG Qing-zhou, CUI Chun-xiang, YIN Fu-xing, JI Xiang-wei. Effect of combined addition of Al−Ti−B ribbon and Zr element on the microstructure, mechanical and damping properties of ZA22 alloy [J]. Materials & Design, 2017, 127: 97−105.

[14] LUO B H, BAI Z H, XIE Y Q. The effects of trace Sc and Zr on microstructure and internal friction of Zn−Al eutectoid alloy [J]. Materials Science and Engineering A, 2004, 370: 172−176.

[15] SAFWAN M A, ADNAN I O. Effect of Mo addition to ZA22 alloy grain refined by Ti−B on its metallurgical and mechanical characteristics in the as cast condition [J]. Materials Science Forum, 2017, 886: 64−68.

[16] DING Jin-hua, CUI Chun-xiang, SUN Yi-jiao, SHI Jie-jie, CUI Sen, MA Qing. Preparation of in situ Al_3Nb−NbB_2−NbC/Al inoculant and its effect on microstructures and properties of weldable Al−Cu−Mn alloy [J]. Materials Science and Engineering A, 2018, 738: 273−282.

[17] ZHUO Zi-ming, MAO Hong-kui, XU Hong, FU Yi-zheng. Density functional theory study of Al/NbB_2 heterogeneous nucleation interface [J]. Applied Surface Science, 2018, 456: 37−42.

[18] LIU Shui-qing, CUI Chun-xiang, WANG Xin, HAN Chong, CHEN Heng-li, SHI Jie-jie. Interfacial microstructure and nucleating mechanism of melt-spun CeB_6/Al composite inoculant [J]. Applied Surface Science, 2018, 431: 202−206.

[19] LIU Shui-qing, WANG Xin, CUI Chun-xiang, ZHAO Li-chen, LI Nuo, ZHANG Zhe, DING Jin-hua, SHA Deng-hao. Enhanced grain refinement of in situ CeB_6/Al composite inoculant on pure aluminum by microstructure control [J]. Journal of Alloys and Compounds, 2017, 701(15): 926−934.

[20] LIU Shui-qing, WANG Xin, TAO You-rui, HAN Xu, CUI Chun-xiang. Enhanced corrosion resistance of 5083 aluminum alloy by refining with nano-CeB_6/Al inoculant [J]. Applied Surface Science, 2019, 484: 403−408.

[21] XU J, LI Y, HU B, JIANG Y, LI Q. Development of Al−Nb−B master alloy with high Nb/B ratio for grain refinement of hypoeutectic Al−Si cast alloys [J]. Journal of Materials Science, 2019, 54(23):14561−14576.

[22] JIAO Zhi-xian, WANG Qing-zhou, YIN Fu-xing, CUI Chun-xiang, ZHANG Jian-jun, YAO Chang. Effects of $Cu_{51}Zr_{14}$ inoculant and caliber rolling on microstructures and comprehensive properties of a Cu−Al−Mn shape memory alloy [J]. Materials Science and Engineering A, 2020, 772: 138773.

[23] WU X Y, ZHANG H R, JIANG F, YUN Y, JIA L N, ZHANG H. Microstructure and grain refinement performance of a new Al−5Nb−RE−B master alloy [J]. Rare Metal Materials and Engineering, 2018, 47: 2017−2022.

[24] NOWAK M, BOLZONI L, BABU N H. Grain refinement of Al−Si alloys by Nb−B inoculation. Part I: Concept development and effect on binary alloys [J]. Materials & Design, 2015, 66: 366−375.

[25] ZHANG M X, KELLY P M, EASTON M A, TAYLOR J A. Crystallographic study of grain refinement in aluminum alloys using the edge-to-edge matching model [J]. Acta Materialia, 2005, 53: 1427−1438.

[26] JING Li-jun, PAN Ye, LU Tao, PI Jin-hong, GU Teng-fei. Nucleation potency prediction of LaB_6 with E2EM model and its influence on microstructure and tensile properties of Al−7Si−0.3Mg alloy [J]. Transactions of Nonferrous Metals Society of China, 2018, 28(9): 1687−1694.

[27] ZHANG M X, KELLY P M. Understanding the crystallography of the eutectoid microstructure in a Zn−Al alloy using the edge-to-edge matching model [J]. Scripta Materialia, 2006, 55: 577−580.

Al−10Nb−3Ce−2.5B 孕育剂对 Zn−Al 共析合金显微组织、阻尼和拉伸力学性能的影响

张建军[1]，殷福星[2]，余 晖[1]，冀璞光[1]，刘 力[1]，李玉芳[1]，焦志娴[1]，王清周[1]

1. 河北工业大学 材料科学与工程学院 天津市材料层状复合与界面控制技术重点实验室，天津 300130；
2. 广东省科学院 新材料研究所，广州 510651

摘 要：制备一种新型 Al−10Nb−3Ce−2.5B 孕育剂，并系统研究其对锌铝共析(ZA22)合金显微组织、阻尼和拉伸力学性能的影响。结果表明，该孕育剂对 ZA22 合金中的 α 相具有显著的细化作用(α 相最低可被细化至约 16 μm)，并可使得 α 相的形貌从粗大枝晶状转变为细小花瓣状。通过边−边匹配晶体学模型(E2EM)建立孕育剂中 CeB_6 和 NbB_2 颗粒与 α 相之间的位向关系(ORs)，并基于该 E2EM 模型揭示孕育剂对 ZA22 合金的细化机理。与未细化 ZA22 合金相比，孕育细化 ZA22 合金的高温阻尼性能，特别是逆共析转变阻尼峰得到显著提升。此外，孕育细化 ZA22 合金的室温拉伸力学性能也得到了显著提高，具有最佳细化效果的 ZA22 合金的抗拉强度和伸长率分别比未细化 ZA22 合金的高 18.56%和 119.04%。对相关机理进行了讨论。

关键词：Zn−Al 共析合金；孕育剂；显微组织细化；阻尼；拉伸力学性能

(Edited by Xiang-qun LI)